Check for updates

Small

NANO · MICRO small
www.small-journal.com

RESEARCH ARTICLE OPEN ACCESS

PDA-Engineered 3D-Printed Polymer–ZrO_2 Hybrid Scaffolds Enabling Enhanced Radiopacity, Photothermal Therapy, and Cell Migration Modulation

Sumin Kang[1] | Yun-Jin Jeong[2] | Seokjae Kim[3,4] | Van Du Nguyen[5] | Songah Jeong[1] | Juyeong Jo[4] | Arunkumar Shanmugasundaram[3] | Jin Uk Jeong[1] | Dong-Weon Lee[3] | Eunpyo Choi[5] | Hyungwoo Kim[1]

[1]School of Polymer Science and Engineering, Chonnam National University, Gwangju, South Korea | [2]Department of Automatic System Engineering, Chosun College of Science & Technology, Gwangju, South Korea | [3]School of Mechanical Engineering, Chonnam National University, Gwangju, South Korea | [4]Korea Institute of Medical Microrobotics, Gwangju, South Korea | [5]Department of Mechanical Engineering, Sogang University, Seoul, South Korea

Correspondence: Dong-Weon Lee (mems@jnu.ac.kr) | Eunpyo Choi (echoi@sogang.ac.kr) | Hyungwoo Kim (kimhw@jnu.ac.kr)

Received: 23 January 2026 | **Revised:** 11 August 2026 | **Accepted:** 19 August 2026

Keywords: 3D printing | poly(ε-caprolactone) (PCL) | polydopamine (PDA) coating, polymer scaffold | ZrO_2

ABSTRACT

The clinical translation of bioresorbable polymer scaffold is limited by radiolucency, insufficient mechanical strength, and the absence of post-implantation therapeutic control. This study introduces a multifunctional scaffold that addresses these challenges through a polymer–ceramic nanocomposite architecture and bioinspired surface modification. ZrO_2 nanoparticles are uniformly embedded into poly(ε-caprolactone) (PCL) via solution blending and fabricated into vascular scaffold by fused deposition modeling, yielding improved elastic modulus and radial strength while preserving elastic recovery. The ceramic phase provides intrinsic and sustained x-ray visibility in vitro, in vivo, and during 100-day perfusion, outperforming conventional contrast-agent-based strategies. A subsequent polydopamine (PDA) coating step enables efficient near-infrared (808 nm) photothermal functionality, which was leveraged for photothermal therapeutic modulation and repeatable, pulse-controlled release of paclitaxel. Cellular evaluation of vascular smooth muscle cell viability and migration underscores the therapeutic relevance of this externally triggered strategy for restenosis prevention. Overall, by integrating mechanical reinforcement, x-ray imaging capability, and remote therapeutic activation within a single PCL-based hybrid platform, this system addresses the long-standing clinical limitations of polymeric vascular scaffolds and offers a promising strategy for next-generation theranostic vascular implants.

1 | Introduction

Additively manufactured polymeric scaffolds offer a key approach for minimally invasive implantation, tissue regeneration, and localized therapy, owing to their structural tunability and clinical practicality [1–4]. However, despite considerable progress in scaffold design and fabrication, polymer-based implants remain fundamentally constrained by their inability to support image-guided implantation or facilitate active post-implantation control [5, 6]. In particular, the intrinsic radiolucency of most biodegradable polymers impedes accurate intraoperative positioning and long-term monitoring using x-ray-based imaging, which remains the predominant modality in interventional medicine [7, 8]. Simultaneously, polymeric scaffolds typically act as passive drug reservoirs, relying on diffusion-driven release with limited spatial and

Sumin Kang, Yun-Jin Jeong and Seokjae Kim contributed equally to this work.

This is an open access article under the terms of the Creative Commons Attribution-NonCommercial License, which permits use, distribution and reproduction in any medium, provided the original work is properly cited and is not used for commercial purposes.
© 2026 The Author(s). *Small* published by Wiley-VCH GmbH

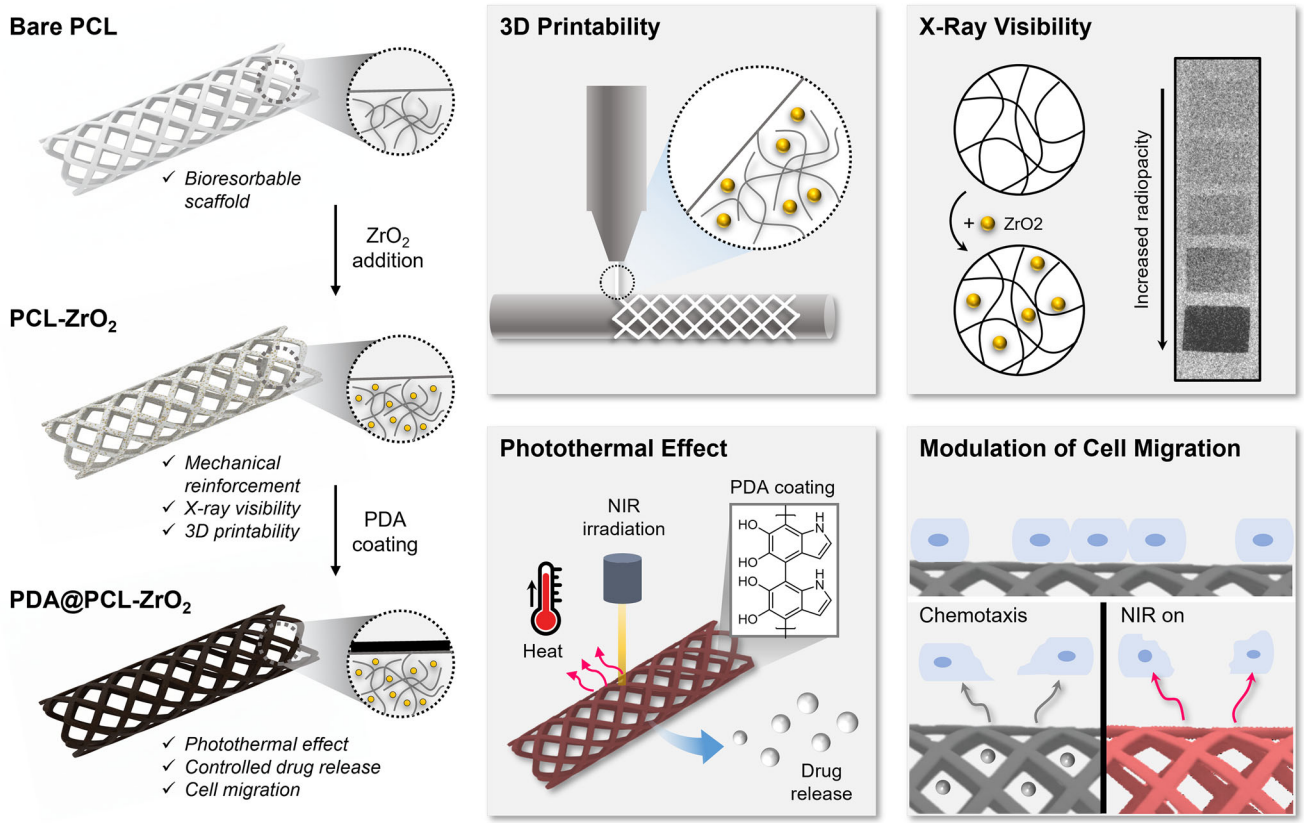


FIGURE 1 | Overview of the design concept and multifunctional performance of the surface-engineered 3D-printed composite scaffold, illustrating (left) the fabrication strategy and (right) the resulting functional properties.

temporal control. Furthermore, their bioinert surfaces lack the functionality to modulate the cellular microenvironment required for effective tissue regeneration [9–11].

So far, attempts to address these limitations have typically targeted individual challenges in isolation, often compromising clinical feasibility. For instance, radiopacity has been achieved using iodine-based contrast agents or metallic fillers; however, these strategies frequently lead to rapid leaching, cytotoxicity, mechanical mismatch, and reduced printability, thereby hindering long-term implantation and scalable manufacturing [12–14]. In parallel, stimuli-responsive drug delivery systems have been explored in polymer matrices; however, their integration into three-dimensionally (3D) printed scaffolds suitable for clinical use has remained limited, as bulk modification methods often disrupt mechanical integrity and geometric fidelity [15–17]. Consequently, radiographic visibility, controlled therapeutic delivery, and biological interactivity have seldom been realized concurrently within a single, manufacturable polymeric scaffold. Among polymeric materials, poly(ε-caprolactone) (PCL) has garnered widespread attention for 3D-printed biomedical scaffolds owing to its biocompatibility, biodegradability, and favorable regulatory profile [18–21]. However, unmodified PCL is inherently radiolucent and bioinert, lacking the functional motifs necessary for therapeutic modulation or dynamic cell–material interactions [22, 23]. Current strategies for PCL functionalization often involve bulk chemical modifications or complex multi-step processing, which can impair printability, mechanical performance, and scalability—critical parameters for translational manufacturing [24, 25].

Against this background, herein, we develop a multifunctional, 3D-printed PCL scaffold offering enhanced mechanical robustness, intrinsic x-ray visibility, on-demand drug release, and programmable biological interactivity through a unified material and surface engineering approach. Notably, the incorporation of ZrO_2 nanoparticles confers mechanical durability and high radiopacity without compromising 3D printing fidelity or geometric precision [26]. A conformal polydopamine (PDA) coating further functionalizes the scaffold surface, establishing a bioactive interface and simultaneously serving as a photothermal transducer for stimulus-responsive drug delivery [27–29]. This integrated design enables minimally invasive, balloon-expandable deployment with real-time x-ray visualization and postoperative monitoring while also maintaining scaffold integrity during near-infrared (NIR)-triggered, spatiotemporally controlled release of paclitaxel (PTX). In particular, the combined effects of surface bioactivation and NIR responsiveness markedly regulate cell migration, highlighting the clinical potential of this platform to modulate the cellular microenvironment after implantation (Figure 1). Collectively, this system advances traditional polymeric scaffolds beyond passive structural roles toward image-visible, stimuli-responsive, and biologically interactive implants, offering a scalable strategy for next-generation imaging-based regenerative and therapeutic applications.

16136829, 2026, 61, Downloaded from https://onlinelibrary.wiley.com/doi/10.1002/smll.75502 by Sogang University, Wiley Online Library on [04/11/2026]. See the Terms and Conditions (https://onlinelibrary.wiley.com/terms-and-conditions) on Wiley Online Library for rules of use; OA articles are governed by the applicable Creative Commons License

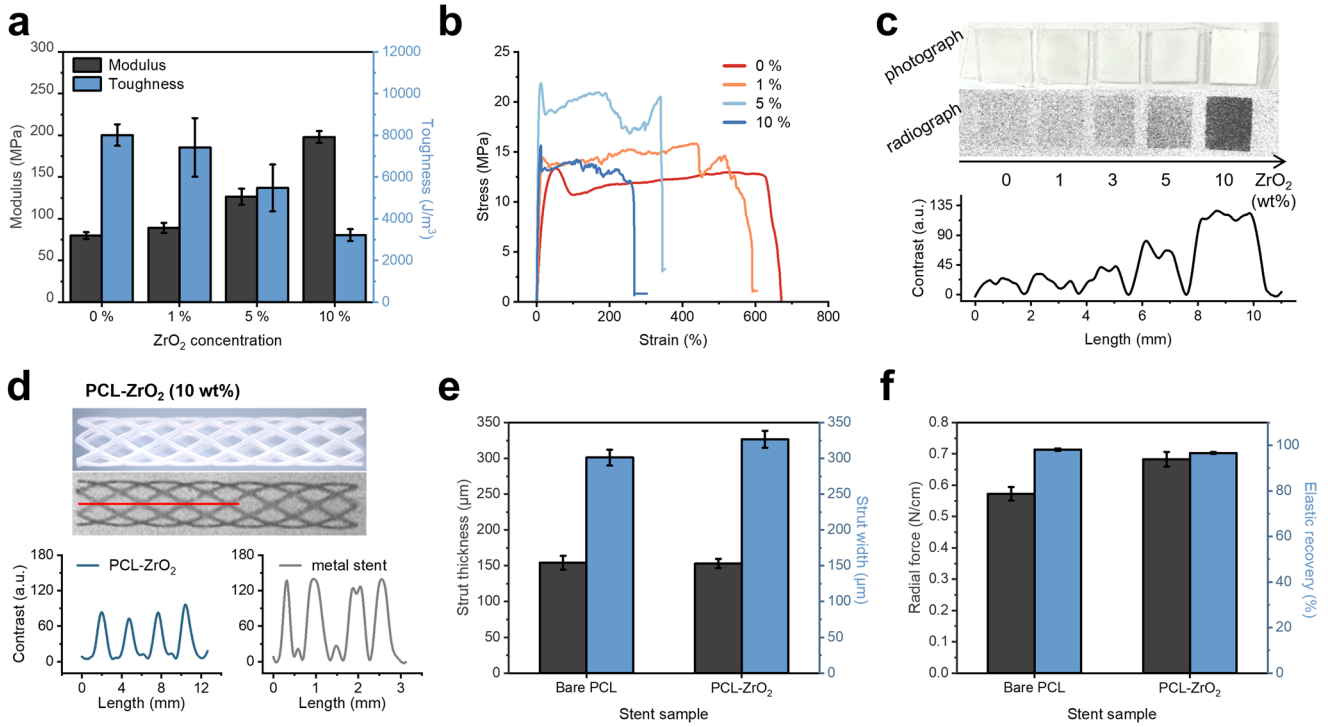


FIGURE 2 | Characterization of the fabricated PCL–ZrO_2 scaffolds. (a) Elastic moduli and toughness of the ZrO_2-reinforced PCL composite films; (b) representative tensile stress–strain curves. (c) (top) Photographs and radiographs of ZrO_2 composites with increasing ZrO_2 content; (bottom) corresponding grayscale contrast intensities derived from radiographs. (d) Fabrication of the 3D-printed PCL–ZrO_2 scaffold: (top) photograph and radiograph; (bottom) radiographic contrast profiles of PCL–ZrO_2 struts along a red line (left) and a clinical metal stent for comparison (right). (e, f) Structural and mechanical evaluation of the bare PCL and PCL–ZrO_2 scaffolds. (e) Quantitative comparison of strut dimensions for the bare PCL and PCL–ZrO_2 scaffolds. (f) Radial force and elastic recovery rate, both normalized by scaffold length, indicating improved radial strength upon ZrO_2 reinforcement. All data are presented as the mean ± 95% confidence interval (CI) from four independent samples ($n = 4$).

2 | Results and Discussion

2.1 | Fabrication and Characterization of ZrO_2-Loaded PCL Nanocomposite Scaffolds

To achieve uniform dispersion of ZrO_2 nanoparticles, specified amounts of these nanoparticles (0–10 wt%) were incorporated into a PCL solution in dichloromethane (DCM), followed by precipitation to obtain the nanocomposite. Owing to the thermoplastic nature of PCL, nanocomposite films were easily fabricated via hot pressing at approximately 60 °C, and their mechanical properties were evaluated through tensile testing. At concentrations exceeding 10 wt%, the ZrO_2 nanoparticles exhibited visible agglomeration within the composite films. Overall, the addition of ZrO_2 nanoparticles reinforced the PCL matrix (Figure 2a), with its elastic modulus increasing proportionally to nanoparticle content. For instance, at 10 wt% ZrO_2, the elastic modulus reached approximately 0.2 GPa, which is approximately 2.5 times greater than that of neat PCL. In contrast, composite toughness declined with increasing ZrO_2 content, owing to the formation of additional physical cross-links at the nanoparticle–polymer interface, which stiffened the PCL matrix, consistent with prior reports [30–32]. Representative tensile stress–strain profiles for the composites are shown in Figure 2b.

In parallel, the incorporation of ZrO_2 substantially enhanced the x-ray visibility of PCL. While bare PCL films were nearly transparent and radiolucent, the addition of ZrO_2 rendered the films more translucent and radiopaque, primarily owing to the photoelectric properties of Zr atoms. Figure 2c presents representative photographs and radiographs of the composite films, illustrating the corresponding increase in radiographic contrast. Radiopacity increased proportionally to ZrO_2 content and became clearly detectable at ZrO_2 contents above 3 wt%.

Based on the mechanical properties and radiographic visibility outlined above, a composite scaffold containing 10 wt% ZrO_2/PCL (PCL–ZrO_2) was fabricated using a fused-deposition-modeling (FDM)-based 3D printing system (Figure S1) [5, 33]. Owing to the increased melt viscosity of PCL–ZrO_2, its 3D printing could be performed at lower temperature of 130°C yet with higher extrusion pressure of 0.65 MPa, compared to the case of bare PCL (175°C and 0.6 MPa). As depicted in Figure 2d, the PCL–ZrO_2 scaffold was fabricated without strut discontinuities and displayed strong radiopacity during real-time x-ray imaging. Notably, the radiographic visibility of the PCL–ZrO_2 struts approached that of a clinical metal stent, reaching over 70% of its contrast intensity. The corresponding radiograph of the metal stent is presented in Figure S2.

The geometric characteristics of scaffold struts critically influence the mechanical performance, flexibility, and biological response of PCL-based hybrid scaffolds. Accordingly, the strut thickness and width of both the bare PCL and PCL–ZrO_2 scaffolds were

16136829, 2026, 61, Downloaded from https://onlinelibrary.wiley.com/doi/10.1002/smll.75502 by Sogang University, Wiley Online Library on [04/11/2026]. See the Terms and Conditions (https://onlinelibrary.wiley.com/terms-and-conditions) on Wiley Online Library for rules of use; OA articles are governed by the applicable Creative Commons License

measured (Figure 2e). The average strut thickness of the bare PCL scaffold was 154.2 ± 9.7 μm, while that of the ZrO_2-reinforced scaffold was 153.3 ± 6.3 μm. The bare PCL scaffold exhibited a mean width of 301.1 ± 11.1 μm, whereas the PCL–ZrO_2 scaffold showed a greater width of 326.6 ± 11.8 μm. This widening is likely attributable to the increased viscosity and altered melt rheology of the composite during extrusion-based printing, which influences the lateral spreading of deposited filaments.

The radial force of a vascular scaffold is a key biomechanical property governing its ability to maintain vessel patency, resist external compressive forces, and enable accurate deployment during interventional procedures. An adequate radial force is required to counteract vessel recoil and support lumen expansion, thereby improving long-term clinical outcomes. To quantitatively assess the radial force of scaffolds fabricated from bare PCL and PCL-ZrO_2, a compression resistance test was performed using a universal testing machine configured with a parallel plate setup. In this test, each scaffold was placed between two flat compression plates, and the upper plate was lowered at a constant displacement rate of 0.1 mm s^{-1} until the scaffold experienced measurable deformation. The corresponding compressive force was recorded as a function of displacement.

The pristine PCL scaffold exhibited a radial force of 0.57 ± 0.02 N cm^{-1}. However, upon incorporation of 10 wt% ZrO_2 nanoparticles, the composite scaffold demonstrated a notable increase in radial force, measuring 0.68 ± 0.02 N cm^{-1} (Figure 2f). This improvement in mechanical strength was attributed to the reinforcing effect of the ceramic fillers, which enhanced the scaffold's stiffness and resistance to radial deformation under compression. Elastic recovery, which reflects a scaffold's ability to regain its original dimensions after deformation, is another key parameter in polymer-based designs. A high degree of elastic recovery is crucial to maintaining scaffold integrity under the cyclic loading conditions of dynamic biological environments such as vascular systems. To evaluate the elastic recovery performance of the fabricated scaffolds containing bare PCL and PCL–ZrO_2, radial compression tests were performed using a customized setup integrated with a universal testing system. Each scaffold (18 mm in length and 3 mm in diameter) underwent a controlled compression protocol, with compression applied at a rate of 1 mm min^{-1} until a total deformation of 1.5 mm was reached. The compressed state was maintained for 30 s to simulate sustained mechanical loading, after which the compression head was retracted at the same rate to allow the scaffold to recover. The elastic recovery rate (R) was calculated as the percentage of the scaffold diameter after recovery (d) relative to the initial, pre-compression diameter (D), using the formula: $R = (d/D) \times 100\%$. Notably, both the bare PCL and PCL–ZrO_2 scaffolds demonstrated high recovery, returning to 98.14 ± 0.55% and 96.63 ± 0.41% of their original diameter, respectively, following initial compression (Figure 2f). This performance remained consistent over five consecutive compression–recovery cycles, indicating strong mechanical resilience and shape memory characteristics. The incorporation of 10 wt% ZrO_2 nanoparticles did not considerably alter the elastic recovery rate, suggesting that the reinforcement did not compromise scaffold elasticity or flexibility under cyclic loading.

2.2 | PDA Coating for the Functionalized PDA@PCL–ZrO_2 Scaffolds

To enable further functionalization, the PCL–ZrO_2 scaffold was coated with a thin layer of PDA under aqueous conditions, following a previously reported method [34, 35], yielding a PDA@ PCL–ZrO_2 scaffold. This surface modification conferred photothermal activity without compromising intrinsic physical properties or causing structural deformation. The PDA coating produced a visible brown color (top, Figure 3a). Next, to assess the effect of PDA coating on mechanical properties, a PDA@PCL–ZrO_2 film was fabricated and subjected to tensile testing. This coated film exhibited approximately a twofold increase in elongation at break, along with slight improvements in elastic modulus and toughness, relative to the uncoated film (bottom, Figure 3a). These reinforcing effects on the PCL matrix likely arise from the synergistic combination of ZrO_2 nanoparticles and the PDA outer coating layer, leading to polymer chain mobility restriction and yield strength enhancement.

X-ray imaging under both dry and wet conditions confirmed that the metal stent, as expected, exhibited the highest radiopacity (Figure 3b). In parallel, the PDA@PCL–ZrO_2 scaffold also exhibited clear x-ray visibility in air and underwater, indicating that ZrO_2 incorporation effectively enhanced radiopacity. Accordingly, the struts of the composite scaffold remained highly discernible under x-ray exposure in both conditions, similar to the metal stent. The control PCL scaffold loaded with iohexol also displayed enhanced visibility in air compared to bare PCL, owing to the presence of iohexol, a commercial radiopaque agent. However, its visibility was no longer distinguishable underwater, in contrast to the PDA@PCL–ZrO_2 and metal stents. These results indicate that stable integration of ZrO_2 fillers into the PCL matrix ensures reliable x-ray detectability of the scaffold under various procedural conditions.

Furthermore, the mechanical performance of the bare PCL and PDA@PCL–ZrO_2 scaffolds was systematically evaluated under simulated balloon-expandable deployment conditions to evaluate their clinical suitability as vascular scaffolds. As illustrated in Figure 3c,d, the scaffolds were crimped onto balloon catheters and subjected to controlled expansion using a radial compression testing system (Model RJ, Blockwise) under balloon-expansion conditions (30°C, 15 psi). During crimping, both scaffold types exhibited excellent compressibility, with their diameters dropping from ~3.13 mm to ~1.45 mm, enabling facile delivery through minimally invasive systems. Following balloon expansion, the scaffolds regained their original geometry, achieving diameters of 3.02 ± 0.05 mm (bare PCL) and 2.98 ± 0.06 mm (PDA@PCL–ZrO_2), demonstrating effective radial responsiveness and minimal strut deformation. After balloon deflation, both the PCL (2.42 ± 0.03 mm) and PDA@PCL–ZrO_2 (2.43 ± 0.06 mm) scaffolds maintained a stable expanded geometry, exhibiting comparable recovery behavior. Overall, PDA@PCL–ZrO_2 displayed a strut geometry comparable to that of bare PCL, indicating that the nanocomposite retained mechanical recovery characteristics similar to those of pure PCL. Further, optical images confirmed the structural integrity and deformation behavior of the fabricated vascular scaffolds throughout deployment (Figure 3c). In the crimped state, both scaffolds exhibited a

16136829, 2026, 61, Downloaded from https://onlinelibrary.wiley.com/doi/10.1002/smll.75502 by Sogang University, Wiley Online Library on [04/11/2026]. See the Terms and Conditions (https://onlinelibrary.wiley.com/terms-and-conditions) on Wiley Online Library for rules of use; OA articles are governed by the applicable Creative Commons License

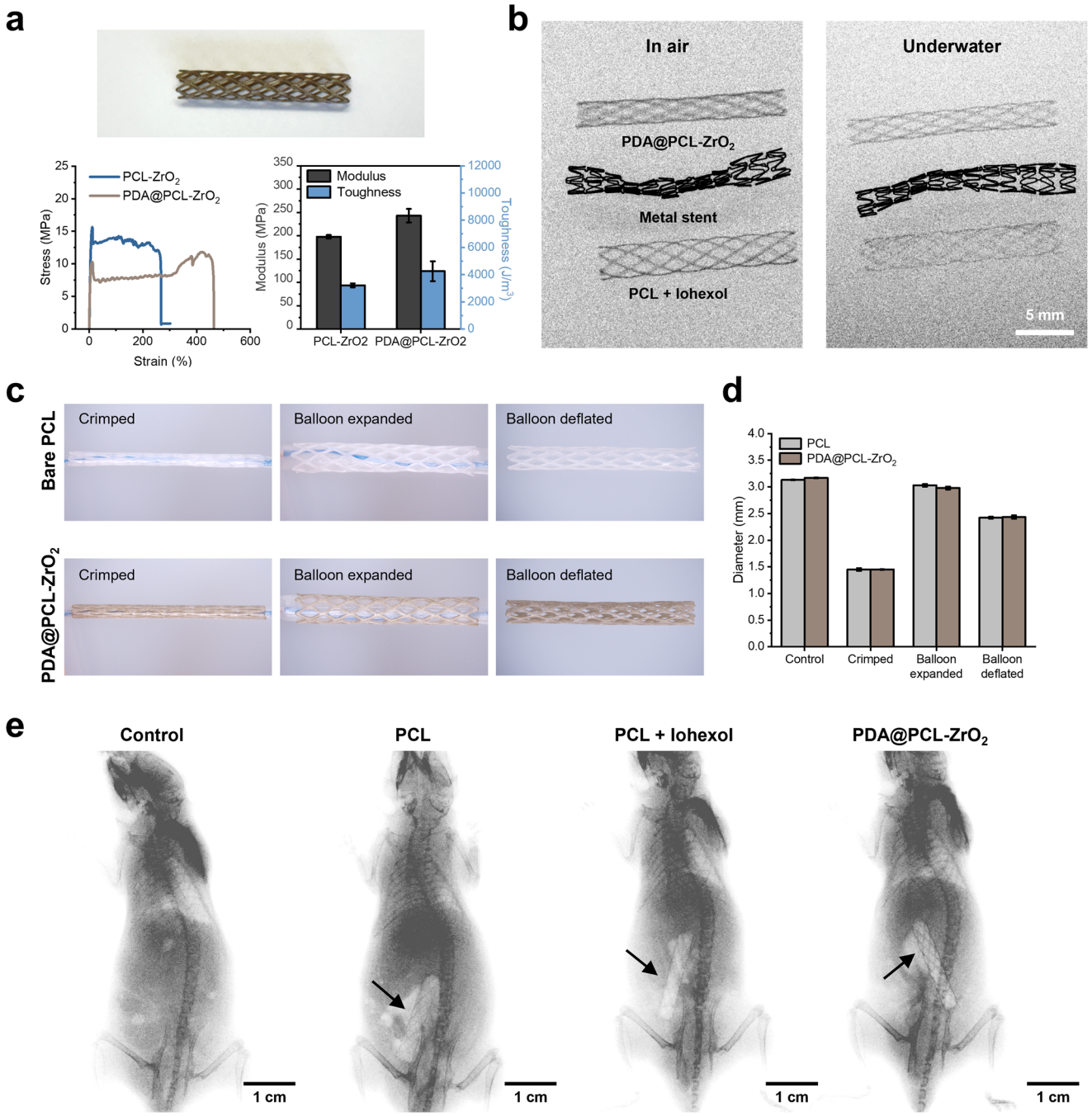


FIGURE 3 | Evaluation of the PDA@PCL–ZrO_2 scaffold. (a) (top) Photograph of the PDA@PCL–ZrO_2 scaffold; (bottom) tensile stress–strain curves of PCL–ZrO_2 and PDA@PCL–ZrO_2 (left) and comparison of their elastic modulus and toughness (right). (b) In vitro x-ray images of the PDA@PCL–ZrO_2 scaffold in the dry (left) and wet (right) states. Dry: tube voltage 100 kV, tube current 120 mA; Wet: tube voltage 80 kV, tube current 160 mA. The metal stent and the PCL scaffold containing iohexol were included for comparison. (c) Optical images of the bare PCL and PDA@PCL–ZrO_2 scaffolds at different deployment stages: crimped, balloon-expanded, and balloon-deflated. (d) Quantitative diameter measurements of the scaffolds at each stage of deployment. All statistical data are presented as the mean ± 95% CI from four independent samples ($n = 4$). (e) In vivo x-ray images of mice implanted with different scaffolds (from left to right: bare PCL, PCL containing iohexol, PDA@PCL–ZrO_2; $n = 1$ mouse per group, qualitative assessment). Arrows indicate the locations of the implanted scaffolds ($n = 1$ per group).

compact configuration with well-aligned struts, reflecting high flexibility and compatibility with balloon catheter systems. Upon balloon expansion, the scaffolds demonstrated uniform radial dilation with a well-defined open-cell mesh architecture. The struts expanded symmetrically without any signs of fracture or collapse, underscoring the mechanical resilience of the scaffolds. After balloon deflation, the scaffolds marginally recoiled while preserving their expanded configuration.

The measured diameters are presented in Figure 3d. These data confirm that the embedded 10 wt% ZrO_2 and PDA coating still preserved expansion behavior without critically compromising

16136829, 2026, 61, Downloaded from https://onlinelibrary.wiley.com/doi/10.1002/smll.75502 by Sogang University, Wiley Online Library on [04/11/2026]. See the Terms and Conditions (https://onlinelibrary.wiley.com/terms-and-conditions) on Wiley Online Library for rules of use; OA articles are governed by the applicable Creative Commons License

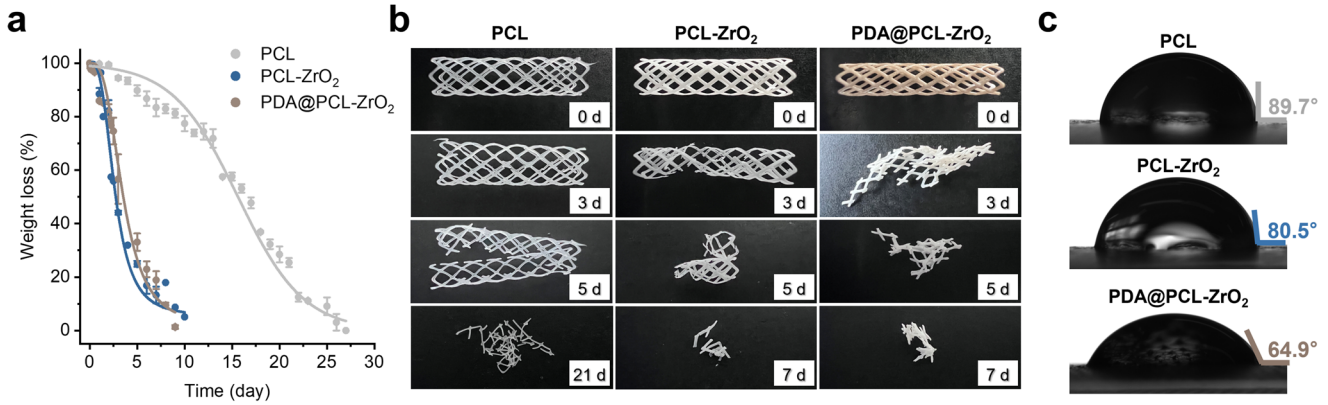


FIGURE 4 | Degradation behavior of PCL-based scaffolds. (a) Change in weight loss of PCL, PCL-ZrO_2, and PDA@PCL-ZrO_2 scaffolds when stored in 5 M NaOH aqueous solution at 40°C. Data are presented as the mean ± 95% CI, calculated from independent samples ($n = 4$). (b) Photographs of each sample during the degradation test taken at different time intervals. (c) Photographs of water droplets on PCL, PCL-ZrO_2, and PDA@ PCL-ZrO_2 films.

the scaffold's radial force, which remained at 0.65 ± 0.02 N cm^{-1}. The post-deployment retention capability of PDA@PCL–ZrO_2 is likely attributed to balanced mechanical strength, reduced plastic deformation, and appropriate radial force retention, key factors for maintaining preserving lumen integrity under dynamic physiological loading conditions. These findings indicate that ZrO_2 reinforcement provides a viable strategy for improving the mechanical stability of PCL-based hybrid scaffolds for vascular applications.

X-ray imaging confirmed the visibility of scaffold shape and pattern in the abdominal cavities of mice implanted with bare PCL, iohexol-containing PCL, and PDA@PCL–ZrO_2 scaffolds (Figure 3e). Among these, the PDA@PCL–ZrO_2 scaffold exhibited sharper boundaries and more distinct strut patterns, clearly demonstrating enhanced radiopacity due to ZrO_2 incorporation. These findings suggest that embedding ZrO_2 into biodegradable PCL-based vascular scaffolds improves their in vivo x-ray visibility.

The degradation behavior of the PCL-based scaffolds depending on the incorporation of ZrO_2 and PDA coating was investigated. To evaluate the overall degradation behavior of the scaffolds, an accelerated degradation condition was employed by immersing the scaffolds in a 5 M NaOH aqueous solution and storing them at 40°C. Changes in scaffold weight and overall shape were monitored over time (Figure 4a). The bare PCL scaffold gradually degraded under the basic degradation condition, showing a significant weight loss after 14 days. In contrast, the PCL-ZrO_2 scaffold exhibited a gradual weight loss after 1 day under the degradation conditions, accompanied by substantial collapse of the scaffold structure within 7 days of storage. Likewise, the PDA@PCL-ZrO_2 scaffold underwent similar weight loss and structural collapse. Figure 4b presents time-dependent morphological changes in the PCL, PCL–ZrO_2, and PDA@PCL-ZrO_2 scaffolds during the degradation tests. Consistent with the weight losses, the bare PCL scaffold degraded relatively slowly and remained as fragmented pieces even after 21 days, while both the PCL–ZrO_2 and PDA@PCL–ZrO_2 scaffolds largely lost their original scaffold morphology within 7 days. Water contact angle measurements were also performed to understand the accelerated degradaion behavior (Figure 4c). The bare PCL sample exhibited a contact angle of 89.7°, indicating a relatively hydrophobic surface. Upon incorporation of ZrO_2 nanoparticles, it was slightly reduced to 80.5° presumably due to improved surface hydrophilicity. After PDA coating, PDA@PCL-ZrO_2 showed the lowest contact angle of 64.9°. Taken together, the incorporation of ZrO_2 nanoparticles increased the susceptibility of the scaffold to degradation by facilitating water access through polymer–particle interfaces and increasing the interfacial area exposed to the degradation medium [36]. The PDA coating further enhanced surface wettability and facilitated water penetration into the scaffold, although partial coverage of the ZrO_2 surface may reduce the direct contribution of the exposed nanoparticles. These competing effects likely account for the comparable degradation behavior of the PCL–ZrO_2 and PDA@PCL–ZrO_2 scaffolds.

In addition, the degradation behavior was strongly influenced by the degradation conditions. For example, under pH 7 conditions, negligible degradation was observed from PCL–ZrO_2 over 36 days, whereas degradation in 1 M NaOH proceeded at a substantially slower rate than that in 5 M NaOH, resulting in approximately half of the weight loss over the same period (Figure S3). Following hydrolytic degradation of the PCL matrix, ZrO_2 in the scaffold may be released into the surrounding environment. Although ZrO_2 has been widely utilized in biomedical applications owing to its high biocompatibility and chemical stability [37], its long-term fate and biological impact remain subjects for future investigation.

2.3 | Long-Term X-Ray Visibility of the Scaffolds in a Vascular Phantom

Following the above characterization, the long-term x-ray visibility of PDA@PCL–ZrO_2 was evaluated using a long-term continuous aqueous perfusion model. As illustrated in Figure 5a, the vascular phantom was configured with scaffolds placed between the aortic arch and left coronary artery and continuously perfused with circulating DI water maintained at 36.5°C and 100 mmHg. DI water was used as a simplified aqueous perfusion medium to evaluate the diffusion- and leaching-associated loss of radiopaque agents under long-term flow conditions, while avoiding possible

16136829, 2026, 61, Downloaded from https://onlinelibrary.wiley.com/doi/10.1002/smll.75502 by Sogang University, Wiley Online Library on [04/11/2026]. See the Terms and Conditions (https://onlinelibrary.wiley.com/terms-and-conditions) on Wiley Online Library for rules of use; OA articles are governed by the applicable Creative Commons License

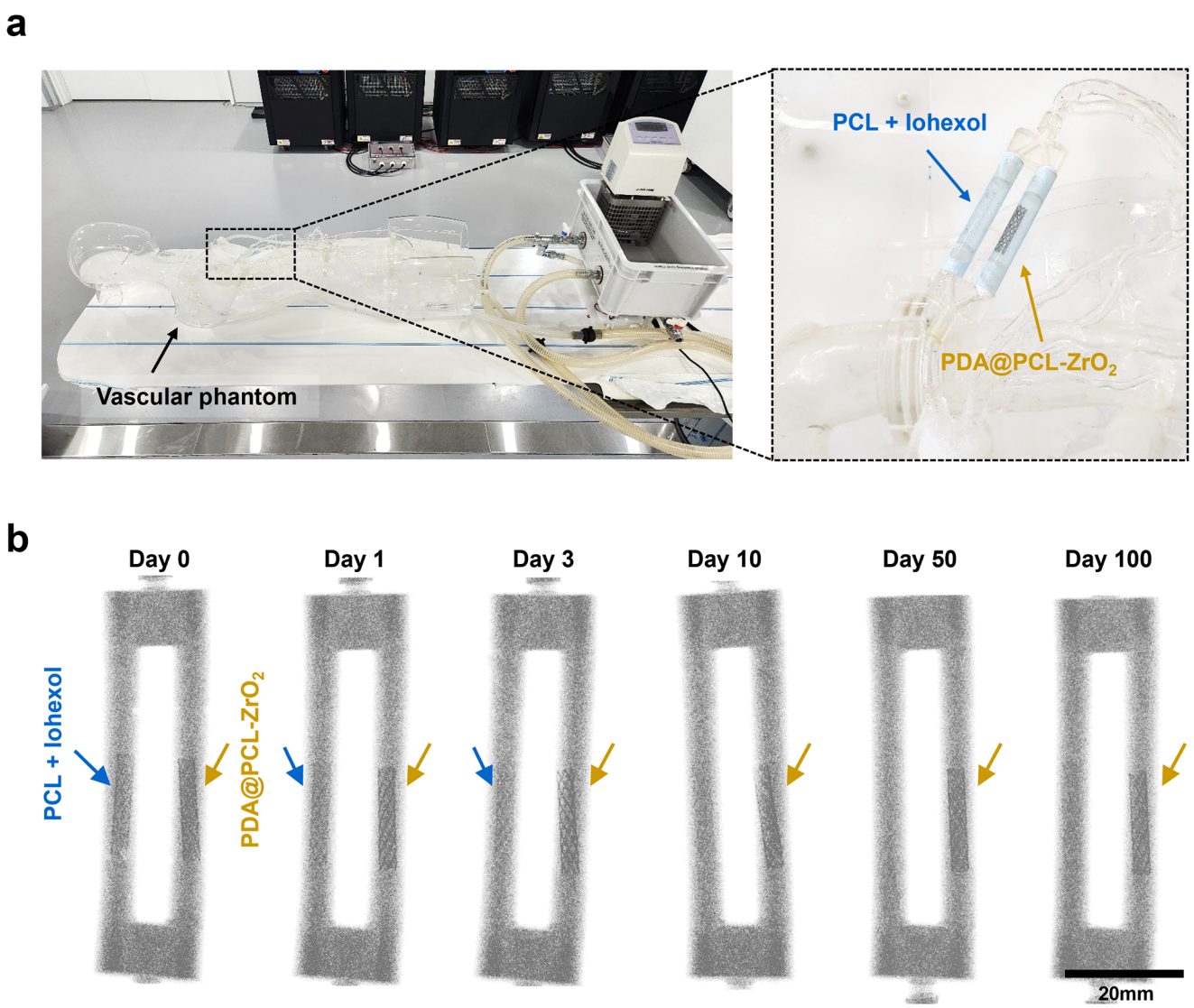


FIGURE 5 | Experimental setup and long-term x-ray visibility of scaffolds in a vascular phantom. (a) Vascular phantom with PDA@PCL–ZrO_2 and iohexol-loaded PCL scaffolds positioned between the aortic arch and the left coronary artery. The phantom was continuously perfused with circulating DI water at 36.5°C under steady-flow conditions. The total phantom-loop flow rate was adjusted to approximately 6.25 L min^{-1} to maintain a pressure of 100 mmHg. (b) X-ray images acquired over 100 days, illustrating a rapid loss of visibility in the iohexol-loaded PCL scaffold (blue) after day 3, in contrast to the PDA@PCL–ZrO_2 scaffolds (gold), which retained clear structural definition throughout the observation period in a single long-term phantom-loop experiment ($n = 1$ experimental run).

effects of viscosity modifiers or blood-mimicking additives on iohexol diffusion. The flow was steady rather than pulsatile, and the total circulation flow rate of the phantom loop was adjusted to approximately 6.25 L/min to maintain the pressure at 100 mmHg. This flow rate represents the overall phantom-loop flow and not the local coronary-branch flow at the scaffold site. Therefore, this model was intended to assess long-term radiopacity retention under continuous aqueous perfusion, rather than to fully reproduce coronary hemodynamics. Radiographic monitoring over 100 days (Figure 5b) revealed a marked difference in radiographic stability between PDA@PCL–ZrO_2 and the control iohexol-loaded PCL scaffolds. Specifically, the PDA@PCL–ZrO_2 scaffolds retained clear structural patterns throughout the 100-day period of continuous aqueous perfusion at 36.5°C, whereas the iohexol-loaded scaffolds exhibited rapid visibility loss, with structural definition fading after day 3 and progressively diminishing thereafter. These results demonstrate that PDA@PCL–ZrO_2 exhibits superior long-term radiopacity retention compared with the iohexol-loaded PCL scaffold, which is susceptible to leaching and diffusion-related loss under long-term continuous aqueous perfusion conditions.

2.4 | Photothermal Responses of the PDA@PCL–ZrO_2 Scaffolds

To evaluate the photothermal response of the PDA@PCL–ZrO_2 scaffold, it was placed in a Petri dish filled with deionized (DI) water and irradiated using an 808 nm NIR laser (left, Figure 6a). Thermal infrared (IR) images acquired before and after 25 min of irradiation revealed a substantial increase in the scaffold's surface temperature (right, Figure 6a). The corresponding temperature

16136829, 2026, 61, Downloaded from https://onlinelibrary.wiley.com/doi/10.1002/smll.75502 by Sogang University, Wiley Online Library on [04/11/2026]. See the Terms and Conditions (https://onlinelibrary.wiley.com/terms-and-conditions) on Wiley Online Library for rules of use; OA articles are governed by the applicable Creative Commons License

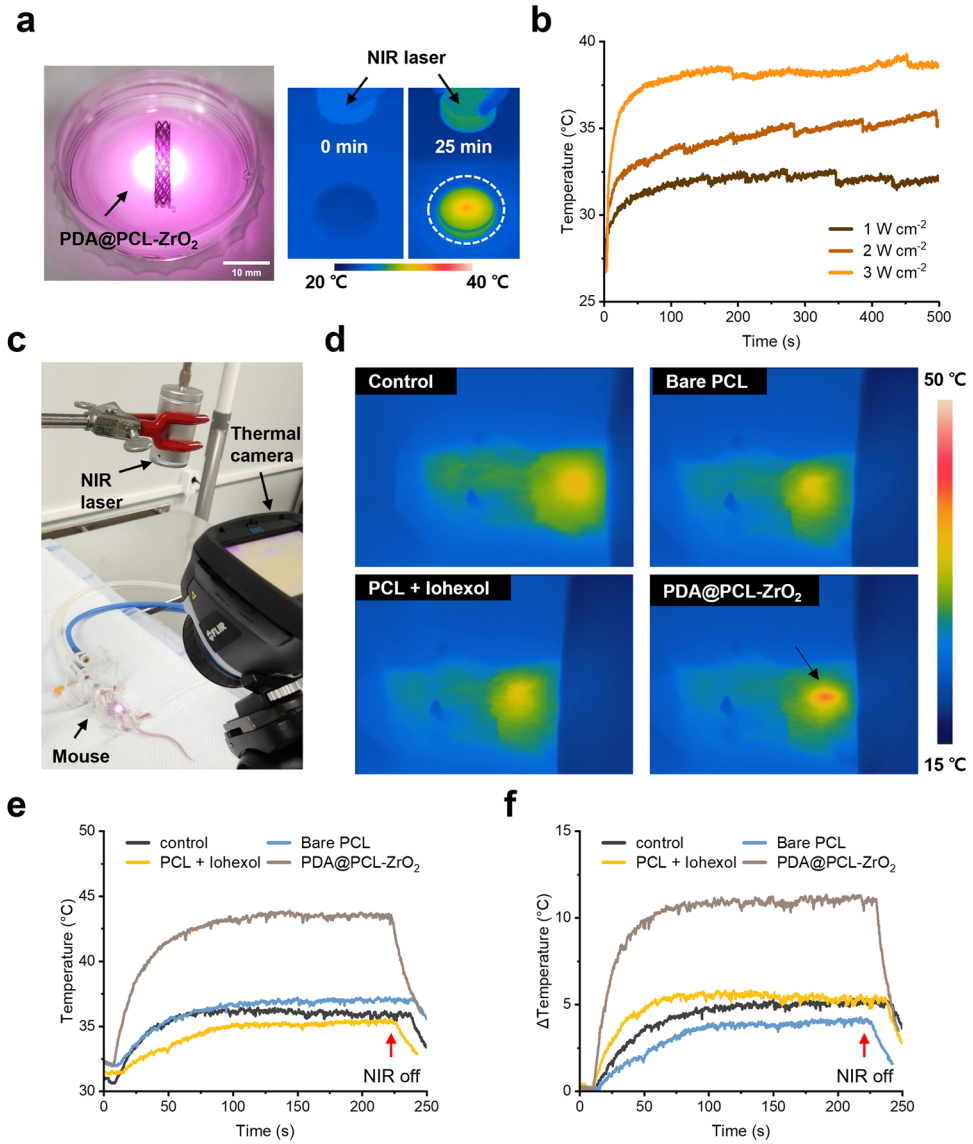


FIGURE 6 | In vitro and in vivo photothermal behavior of polymer scaffolds under NIR irradiation. (a) (left) Photograph of the PDA@PCL–ZrO_2 scaffold placed in a Petri dish filled with DI water and exposed to an 808 nm NIR laser (scale bar: 10 mm). (right) Thermal IR images of the scaffold before and after 25 min of irradiation, illustrating localized heating. (b) Representative temperature profiles of the scaffold under NIR irradiation at different intensities from a single initial in vitro photothermal screening experiment ($n = 1$; no inferential statistical analysis). (c) Experimental setup for the in vivo NIR irradiation of mice. (d) Thermal IR images of control mice and mice implanted with bare PCL, iohexol-loaded PCL, or PDA@PCL–ZrO_2 scaffolds. (e) Absolute temperature changes under NIR irradiation and (f) corresponding ΔT profiles of the control and treated mice. Lines in (e) and (f) represent mean values from three mice per group ($n = 3$ mice per group).

profile is presented in Figure 6b. Notably, the surface temperature increased rapidly, reaching a plateau at ~32.4°C within ~100 s under irradiation at 1 W cm^{-2}, corresponding to a temperature rise (ΔT) of ~6°C. This temperature increase was reproducibly and consistently observed over four consecutive on/off irradiation cycles, confirming the reliable photothermal response of the scaffold (Figure S4). In addition, as the irradiation intensity increased, the equilibrium temperature rose accordingly. For instance, it reached ~35.1°C (ΔT ~9°C) at 2 W cm^{-2} and ~38.4°C (ΔT ~12°C) at 3 W cm^{-2}. This photothermal response confirms the PDA coating's ability to convert NIR light into heat in aqueous environments. Moreover, the induced temperature rise remained within a mild hyperthermic limit, suggesting that the nanocomposite can be applied in in vivo applications such as localized drug release or tissue stimulation without inflicting thermal damage on surrounding tissue.

Figure 6c illustrates the in vivo NIR irradiation setup, with the laser beam precisely aligned with the scaffold implantation site in the abdomen of the mouse. Temperature variation in the mouse was assessed using IR thermography (Figure 6d). For comparison, bare PCL and iohexol-loaded PCL scaffolds were implanted in mice. These scaffolds resulted in only minimal temperature increases after NIR exposure, similar to the control group without scaffolds. In these groups, the heating regions exhibited a circular pattern matching the laser beam diameter. This suggests that the minor temperature increase was likely attributed to NIR absorption by skin chromophores (e.g., melanin

16136829, 2026, 61, Downloaded from https://onlinelibrary.wiley.com/doi/10.1002/smll.75502 by Sogang University, Wiley Online Library on [04/11/2026]. See the Terms and Conditions (https://onlinelibrary.wiley.com/terms-and-conditions) on Wiley Online Library for rules of use; OA articles are governed by the applicable Creative Commons License

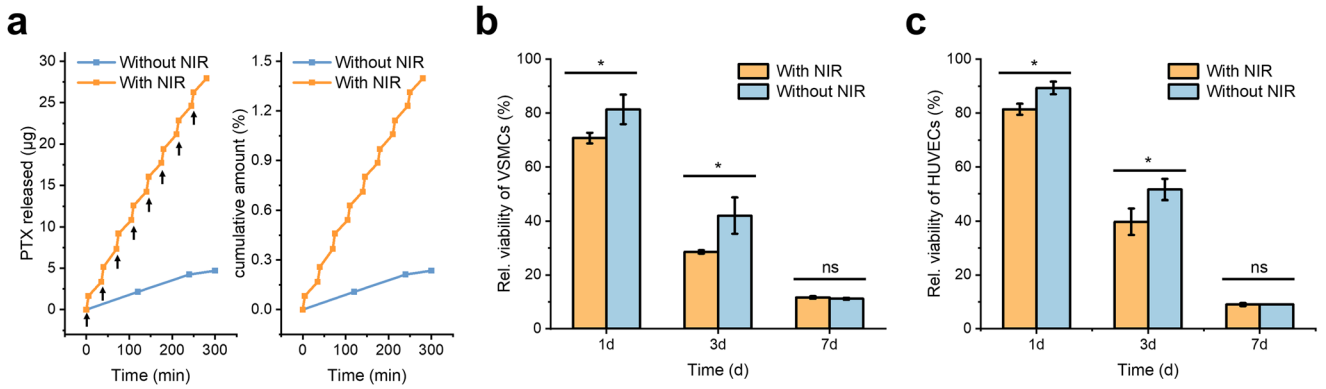


FIGURE 7 | In vitro drug release behavior under NIR stimulation. (a) (left) Absolute amounts of PTX released from PTX-loaded PDA@PCL–ZrO_2 with or without periodic NIR irradiation (arrows indicate irradiation events); (right) corresponding cumulative release percentages. Relative viabilities of (b) VSMCs and (c) HUVECs incubated with eluted media from PTX-loaded PDA@PCL–ZrO_2 membranes in the absence or presence of NIR irradiation over various time points. (*$p < 0.05$; ns, not significant).

and hemoglobin), absorption by underlying tissues, or thermal conduction from adjacent irradiated areas, rather than photothermal conversion by the scaffold material. In contrast, thermal images from the PDA@PCL–ZrO_2 group revealed an elliptical region of localized heating along the scaffold, rather than the circular beam profile, confirming efficient and concentrated photothermal conversion at the implantation site. Additionally, mice implanted with the PDA@PCL–ZrO_2 scaffoldexhibited a faster temperature rise, with ΔT exceeding 10°C and reaching ~41°C, compared to other groups, which showed ΔT values below 5°C (Figure 6e,f).

2.5 | NIR-Triggered Drug Release Behavior

The photothermal response of PDA@PCL–ZrO_2 was further harnessed to enable NIR-responsive drug release. To evaluate this behavior, PTX was incorporated into a PDA@PCL–ZrO_2 membrane, and its release profile was monitored under NIR irradiation *in chemico* using high-performance liquid chromatography (HPLC) (Figure 7a). The PTX content was fixed at 10 wt% relative to PCL for clearer demonstration of release behavior, corresponding to a surface-area-normalized PTX loading of 12.3 μg mm^{-2}. Notably, 10 wt% PTX was uniformly dispersed at the molecular level and encapsulated within the composite matrix to suppress initial burst release and prevent unintended surface leakage. Consequently, in the absence of NIR stimulation, only a negligible amount of PTX (<0.3%) was released from PDA@PCL–ZrO_2 during a 300 min immersion in PBS (pH 7.2) at 37°C. In contrast, NIR irradiation substantially enhanced PTX release. Specifically, after 5 min of exposure, ~1.7 μg of PTX was released from the scaffold, corresponding to a surface-area-normalized release of 0.01 μg mm^{-2}. This response was consistently reproduced over eight consecutive irradiation events, with ~1.7 μg of PTX released per irradiation. This corresponded to ~0.1% of the initial PTX load per irradiation, ultimately resulting in a cumulative release of ~0.7% corresponding to 0.09 μg mm^{-2} after eight irradiations—3.5-fold higher than that observed without NIR exposure. This behavior stems from photothermal heating generated by the PDA layer, which induces localized temperature surges that trigger the release of encapsulated molecules. Because drug release is influenced by scaffold geometry, light intensity, exposure duration, and the resulting local temperature, the PTX release profile can be modulated by adjusting the light irradiation conditions. This suggests that NIR stimulation provides a practical means to tune the amount and timing of drug release from the PDA@PCL–ZrO_2 matrix.

The relative viabilities of vascular smooth muscle cells (VSMCs) and human umbilical vein endothelial cells (HUVECs) exposed to 2 wt% PTX-loaded PDA@PCL–ZrO_2 scaffolds, with or without NIR irradiation, were evaluated over 1, 3, and 7 days, reflecting the number of irradiation events (Figure 7b,c). Because excessive local exposure to PTX can cause cytotoxic effects and delay tissue recovery, a reduced PTX content of 2 wt% was used for the scaffold in the cell experiments. In VSMC viability assays (Figure 6b), NIR irradiation substantially reduced cell viability compared to non-irradiated controls, with the difference most pronounced at day 3. At day 3, the viability was 28.6% with NIR irradiation, compared to 42.0% without it, indicating enhanced cytotoxicity owing to NIR-triggered PTX release. By day 7, cell viability had further declined under both conditions, suggesting a sustained cytotoxic effect from natural PTX release. Meanwhile, in the HUVECs assays, NIR irradiation also reduced cell viability, although to a lesser extent than that in VSMCs (Figure 7c). Specifically, at day 1, HUVEC viability was reduced to 89.3% without NIR exposure and 81.4% with NIR exposure, which further decreased by day 3 to 51.6% and 39.8%, respectively. A sustained cytotoxic effect from passive PTX release was also observed at day 7, by which point most cells had died.

These findings demonstrate the differing effects of applying PTX-loaded scaffolds combined with NIR irradiation on VSMCs and HUVECs. The pronounced cytotoxic effect on VSMCs is clinically desirable, as their excessive proliferation is a major contributor to restenosis following vascular stenting. Specifically, the marked reduction in VSMC viability at an early stage (48–72 h), aligning with the peak proliferation phase, indicates an optimal therapeutic window for NIR-mediated drug release for effective restenosis prevention. Conversely, the reduction in HUVEC viability indicates a potential risk to endothelial integrity under the current experimental conditions. Endothelial healing and re-endothelialization are critical processes for restoring vascular integrity and reducing thrombotic and

16136829, 2026, 61, Downloaded from https://onlinelibrary.wiley.com/doi/10.1002/smll.75502 by Sogang University, Wiley Online Library on [04/11/2026]. See the Terms and Conditions (https://onlinelibrary.wiley.com/terms-and-conditions) on Wiley Online Library for rules of use; OA articles are governed by the applicable Creative Commons License

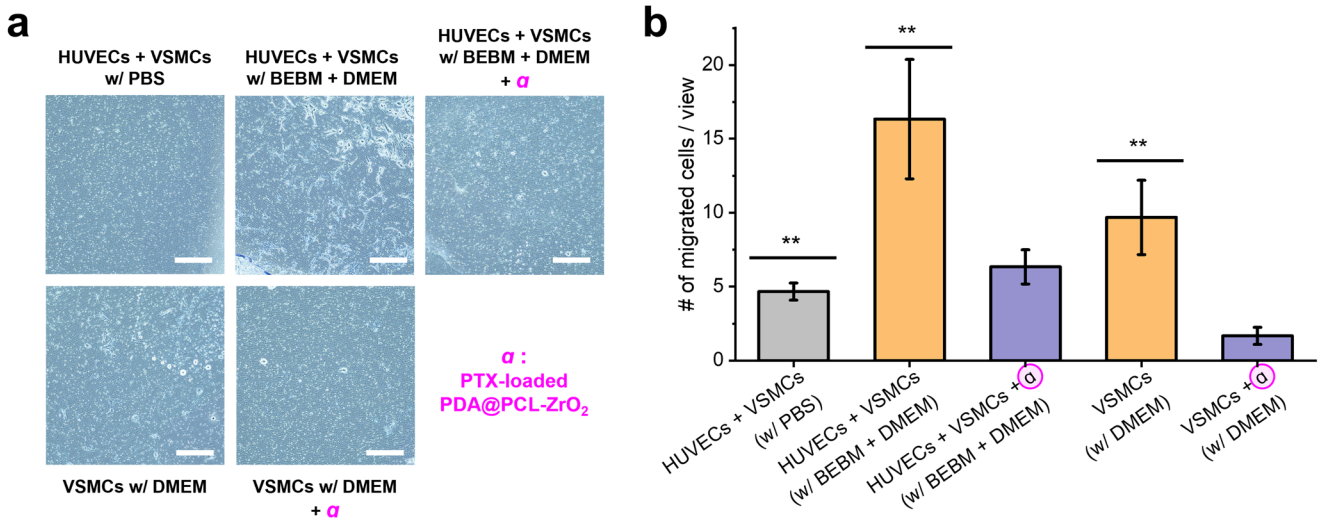


FIGURE 8 | Cellular chemotaxis. (a) Optical images of migrated cells cultured under different conditions (scale bar, 400 μm). (b) Migrated cell counts (**$p < 0.01$).

inflammatory complications after vascular injury [38, 39]. However, the present study did not directly evaluate endothelial recovery, re-endothelialization, or long-term endothelial function; therefore, no definitive conclusion can be drawn regarding the reversibility of the observed HUVEC cytotoxicity. Nevertheless, the overall findings suggest that this scaffold system has potential for NIR-mediated VSMC suppression, but its impact on endothelial preservation requires further investigation. Accordingly, future studies should optimize PTX loading, NIR parameters, and irradiation protocols to enhance selective VSMC suppression while minimizing endothelial cell injury, and should include endothelial recovery assays and in vivo vascular models to assess long-term vascular healing.

In addition, a hemolysis assay was performed to evaluate the hemocompatibility of bare PCL, PDA@PCL–ZrO_2, and PTX-loaded PDA@PCL–ZrO_2 using red blood cells (RBCs) isolated from citrated sheep blood. Hemolysis was evaluated after incubating the samples with the RBC suspension for 1, 3, and 6 h. As shown in Figures S5 and S6, no detectable hemolysis was observed for any of the test films at either concentration or at any incubation time. These results demonstrate excellent hemocompatibility of the fabricated PCL-based hybrid scaffolds with respect to red blood cells.

2.6 | Effect of PDA@PCL–ZrO_2 on Cell Migration Associated With Intimal Hyperplasia

Cellular chemotaxis was investigated, as depicted in Figure 8, which illustrates the directed migration of cells in response to a chemical gradient. To mimic clinical conditions, HUVECs and VSMCs were mixed at a 1:1 cell number ratio and introduced into the upper chamber of Transwell inserts for migration assays. As expected, when phosphate-buffered saline (PBS) was added to the lower chamber, few cells were observed. In contrast, when the co-cultured cells were introduced in the upper chamber and the lower chamber was filled with complete medium, substantial cell migration occurred, indicating positive chemotaxis. Conversely, when the PTX-loaded (2 wt.%) PDA@PCL–ZrO_2 scaffold was added to the medium in the lower chamber, the number of migrated cells was markedly reduced, indicating negative chemotaxis. When the migration assay was conducted using only VSMCs under similar conditions, this negative chemotaxis became more apparent (Figure 8a,b). These findings suggest that PTX may selectively modulate cell migration by disrupting chemotactic signaling or altering the chemoattractant gradient required for directed movement. This observation aligns with the findings of previous studies wherein VSMC chemotaxis was affected by other agents, including Metformin, Luteolin, and MiR155-5p [40–42]. Although the specific mechanism underlying this observation remains under investigation, the inhibitory effects of PTX released from the designed scaffold can effectively regulate VSMC migration, thereby suppressing intimal hyperplasia and alleviating in-stent stenosis.

Immediately after NIR irradiation in the presence of drug-free PDA@PCL–ZrO_2, no discernible morphological differences were observed in VSMCs compared with the non-irradiated control group, as illustrated in Figure 9. However, after 1 day, the number of cells in the irradiated group markedly dropped below that in the non-irradiated group. This difference became more pronounced by day 7, when nearly all cells in the irradiated group had disappeared.

To further investigate the combined effects of PTX and NIR-induced photothermal treatment on the biological responses of VSMCs, an additional experiment was performed in which VSMCs were cultured on PTX-loaded films and subsequently exposed to NIR irradiation under the same conditions described above. Cell morphology was examined immediately after NIR irradiation using Giemsa staining. As shown in Figure S7, VSMCs cultured on PTX-loaded films without NIR irradiation exhibited noticeable morphological changes compared with those cultured on drug-free PDA@PCL–ZrO_2 films under NIR irradiation. Furthermore, NIR irradiation of the PTX-loaded films resulted in more pronounced morphological alterations and a greater reduction in cell density. These observations further support that

16136829, 2026, 61, Downloaded from https://onlinelibrary.wiley.com/doi/10.1002/smll.75502 by Sogang University, Wiley Online Library on [04/11/2026]. See the Terms and Conditions (https://onlinelibrary.wiley.com/terms-and-conditions) on Wiley Online Library for rules of use; OA articles are governed by the applicable Creative Commons License

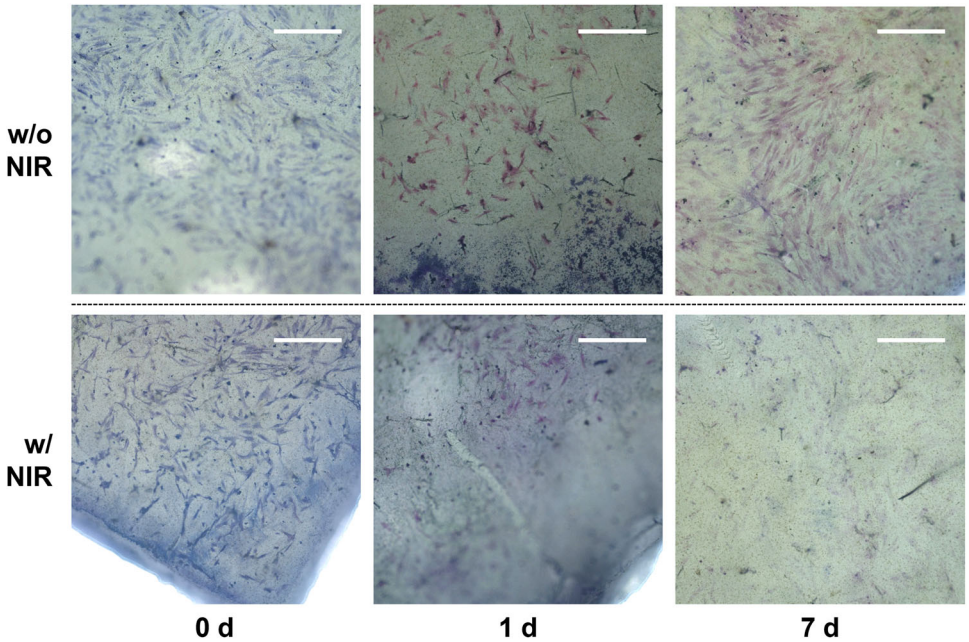


FIGURE 9 | Effect of NIR irradiation on intimal hyperplasia in the presence of PDA@PCL–ZrO_2. Optical images of VSMCs cultured on the drug-free sample without (top) and with (bottom) NIR irradiation at 0, 1, and 7 days (scale bar, 400 μm).

the combined effects of PTX and NIR-induced photothermal treatment exert a stronger inhibitory effect on VSMCs than either treatment alone.

It should be noted that the observed biological responses are likely influenced by both NIR-induced photothermal treatment and PTX release. In the present study, these two mechanisms were partially investigated under separate experimental conditions, including PTX-loaded systems (Figure 7) and drug-free systems under NIR irradiation (Figure 9), indicating that each mechanism can independently influence cellular responses. Furthermore, as demonstrated in the aforementioned experiment (Figure S7), the combined effects of PTX release and NIR-induced photothermal treatment resulted in more pronounced biological responses than either treatment alone. Nevertheless, because these experiments were performed under different experimental configurations, the relative contributions of photothermal heating and PTX release cannot be quantitatively distinguished within the current study. Therefore, the observed biological responses are more appropriately interpreted as arising from the combined effects of photothermal treatment and PTX release, rather than being attributed to a single dominant mechanism.

Given that VSMCs critically influence restenosis by proliferating and migrating, ultimately leading to neointima formation after stenting, the above findings highlight the potential of PDA@PCL–ZrO_2 to ablate VSMCs in the presence of NIR irradiation and thereby reduce in-stent restenosis. Notably, in PDA@PCL–ZrO_2, the PDA layer facilitated the photothermal conversion of NIR light to heat, damaging cell membranes [43]. This effect was not immediately apparent following irradiation; however, by day 7, it became markedly evident, with nearly all cells ablated, likely owing to delayed or subtle stress-induced cellular responses. The underlying time-dependent mechanisms by which the NIR irradiation of PDA@PCL–ZrO_2 induces VSMC apoptosis remain to be elucidated. One proposed mechanism involves the development of NIR-induced mild oxidative stress that activates intracellular signaling cascades to suppress cell proliferation. Another involves the downregulation of proliferation-associated genes in VSMCs (e.g., SOX9, EGR4, and TGFB1), coupled with the upregulation of inhibitory genes (e.g., DNMT1, TIMP3, and PCNA) [44]. Furthermore, the extent of cellular damage or ablation could be modulated by varying the laser intensity, exposure time, and number of irradiation cycles, a topic warranting further investigation.

3 | Conclusion

In summary, we demonstrated a multifunctional PCL-based hybrid scaffold offering sustained radiopacity, photothermal responsiveness, and controlled drug release through a synergistic combination of polymer–ceramic nanocomposite fabrication and bioinspired surface chemistry. Notably, ZrO_2-embedded PCL scaffolds fabricated via 3D printing exhibited substantially improved mechanical performance and sustained x-ray visibility in vitro, in vivo, and under prolonged perfusion, thereby overcoming the inherent limitations of polymer-based scaffolds. Moreover, the PDA coating imparted NIR-induced photothermal functionality, enabling on-demand PTX release and precise modulation of vascular smooth muscle cell proliferation and chemotaxis—two primary contributors to intimal hyperplasia. Overall, by decoupling scaffold mechanics, imaging capabilities, and therapeutic activation into independently tunable components, this platform offers a flexible strategy for designing next-generation vascular biomaterials. In this study, therapeutic efficacy in a vascular restenosis animal model was not directly evaluated. However, key functional elements relevant to restenosis prevention, including NIR-triggered PTX release, reduced VSMC viability, and

16136829, 2026, 61, Downloaded from https://onlinelibrary.wiley.com/doi/10.1002/smll.75502 by Sogang University, Wiley Online Library on [04/11/2026]. See the Terms and Conditions (https://onlinelibrary.wiley.com/terms-and-conditions) on Wiley Online Library for rules of use; OA articles are governed by the applicable Creative Commons License

inhibition of cell migration, were systematically demonstrated. In addition, in vivo photothermal responses and structural visibility were confirmed, indicating that the essential features required for potential therapeutic application can be integrated into a single platform. These findings support the potential of the system as a multifunctional scaffold, although its therapeutic efficacy and long-term vascular response remain to be validated in appropriate animal models. Refining drug dosage, irradiation parameters, and surface chemistry could further enhance cellular selectivity and regenerative efficacy, broadening the potential of this design for a range of implantable biomaterial applications. Although the present study demonstrates the feasibility of integrating radiopacity, photothermal responsiveness, and NIR-triggered drug release into a single PCL-based hybrid scaffold, therapeutic efficacy in vascular restenosis and long-term vascular responses were not directly evaluated. Therefore, further studies using appropriate intravascular implantation models will be required to assess restenosis inhibition, vascular healing, thrombosis-related outcomes, and long-term safety before clinical translation.

4 | Experimental Section

4.1 | Preparation of ZrO_2-Reinforced PCL Composites

ZrO_2-reinforced PCL composites were prepared by dissolving PCL ($M_n = 80$ kDa, $Đ < 2$) with ZrO_2 (particle diameter, 25 nm) at concentrations of 1–10 wt% in DCM (~100 mg mL^{-1}). Each resulting solution was precipitated in diethyl ether and filtered. The composites were vacuum-dried for 1 d and directly employed in scaffold fabrication without further purification.

4.2 | Fabrication of ZrO_2-Loaded PCL Scaffolds Via 3D Printing

Vascular scaffolds comprising bare PCL and PCL reinforced with 10 wt% ZrO_2 nanoparticles (PCL–ZrO_2) were fabricated using a custom-built 3D printing system based on FDM. The bare PCL scaffolds were fabricated by extruding the polymer at 175 °C under a pressure of 0.6 MPa. In contrast, the nanocomposite ink containing 10 wt% ZrO_2 was processed at a lower temperature of 130 °C and a slightly elevated pressure of 0.65 MPa to compensate for the increased viscosity resulting from nanoparticle incorporation. Printing speeds were optimized and maintained at 25% for the bare PCL and 6% for the ZrO_2-reinforced formulation to ensure uniform deposition and structural fidelity. Material deposition was conducted through a dispensing nozzle with an inner diameter of approximately 300 μm, enabling high-resolution strut formation. The scaffolds were printed directly onto a rotating shaft with a diameter of 2.75 mm. Notably, the bare PCL scaffolds exhibited an average strut thickness of 154 μm and a width of 301 μm, whereas the nanocomposite scaffolds displayed a comparable thickness of 153 μm and a slightly broader width of 326 μm, as indicated by optical microscopy. Both scaffold types demonstrated an outer diameter of approximately 3.05 mm and an overall length of 18 mm, aligning with the dimensional specifications for small-diameter vascular interventions.

4.3 | Preparation of PDA-Coated Scaffolds (PDA@PCL–ZrO_2)

Dopamine hydrochloride (50 mg, 0.26 mmol, 5 mg mL^{-1}) was dissolved in 10 mL of Tris buffer (10 mM, pH 8.0) in a 20 mL vial. Following 1 h of stirring, PCL–ZrO_2 scaffolds were added and stirred for an additional 12 h to facilitate PDA coating. The coated samples were subsequently removed, thoroughly rinsed with DI water, and dried in an oven at 60°C for 12 h.

4.4 | In Vitro X-Ray Visibility Test

The x-ray visibility of the scaffolds was evaluated using a previously developed contrast-enhancing formulation containing iohexol. Specifically, commercially available metal stents (TIGER stent, CGBIO Co., Korea) and the fabricated PDA@PCL–ZrO_2 scaffolds were assessed. These scaffolds were placed in 35 mm Petri dishes filled with DI water to simulate wet conditions, while dry-condition imaging was performed without immersion. For comparison, a PCL scaffold containing 10 wt% iohexol was also evaluated [5]. x-ray imaging was performed on an x-ray generator (L9181-02, Hamamatsu Photonics K.K.) coupled with an x-ray detector (C1215A, Hamamatsu Photonics K.K.). This imaging was conducted under the following settings: for dry conditions, tube voltage was 100 kV and current was 120 mA; for wet conditions, voltage was 80 kV and current was 160 mA.

4.5 | In Vivo X-Ray Visibility Test

All animal experiments were conducted with approval from the Institutional Animal Care and Use Committee of the Korea Institute of Medical Microrobotics (KIMIRo-IACUC-2025-R-002). To assess in vivo x-ray visibility, eight-week-old male Balb/c mice underwent midline laparotomy, followed by insertion of the scaffold into the abdominal cavity. The abdominal incision was closed using surgical sutures and tissue adhesive (Vetbond, 3 M). X-ray imaging was conducted using an x-ray generator (L9181-02, Hamamatsu Photonics K.K.) coupled with a detector (C1215A, Hamamatsu Photonics K.K.). Scaffold samples fabricated from bare PCL, iohexol-loaded PCL, and PDA@PCL–ZrO_2 were evaluated comparatively.

4.6 | Long-Term X-Ray Visibility of Scaffolds in a Vascular Phantom

Long-term visibility and retention were examined by comparing PDA@PCL–ZrO_2 with iohexol-loaded PCL scaffolds in a large-vessel phantom. The scaffolds were positioned between the aortic arch and the left coronary artery of an artificial blood vessel phantom (EVE, FAIN-Biomedical). The phantom was perfused with DI water maintained at 36.5 °C using pump module. DI water was selected as a simplified aqueous perfusion medium without viscosity modifiers or blood-mimicking additives, in order to evaluate radiopaque-agent diffusion and leaching under long-term flow conditions. The flow was steady, not pulsatile. A pressure gauge was connected to the brachial artery port of the phantom, and the pump flow rate was adjusted to maintain the overall phantom pressure at 100 mmHg. Under this condition, the

16136829, 2026, 61, Downloaded from https://onlinelibrary.wiley.com/doi/10.1002/smll.75502 by Sogang University, Wiley Online Library on [04/11/2026]. See the Terms and Conditions (https://onlinelibrary.wiley.com/terms-and-conditions) on Wiley Online Library for rules of use; OA articles are governed by the applicable Creative Commons License

total circulation flow rate of the phantom loop was approximately 6.25 L min^{-1}. This value represents the overall loop flow rate and does not directly correspond to the local flow rate at the coronary-branch scaffold site. X-ray imaging was conducted using an x-ray generator (L9181-02, Hamamatsu Photonics K.K.) and a detector (C1215A, Hamamatsu Photonics K.K.) at a tube voltage of 80 kV and a tube current of 160 mA. This imaging was performed periodically throughout a 100-day observation period.

4.7 | Hemolysis test

Red blood cells (RBCs) were isolated from citrated sheep blood (MB-S1876, MBcell, Korea) by centrifugation at 1200 × g for 10 min at 4°C. The RBC pellet was collected and washed twice with cold PBS, followed by dilution with PBS to obtain a final RBC concentration of 5% (v/v). Bare PCL, PDA@PCL–ZrO_2, and PTX-loaded PDA@PCL–ZrO_2 films were immersed in PBS for 24 h to prepare extraction media. Subsequently, 200 μL of each extract was mixed with 800 μL of the prepared RBC suspension in 1.5 mL microcentrifuge tubes, corresponding to film concentrations of 0.5 and 5 mg mL^{-1}. The mixtures were incubated at 37°C for 1, 3, and 6 h. After incubation, the samples were centrifuged at 1200 × g for 5 min, and 100 μL of the supernatant was transferred to a 96-well plate. The absorbance was measured at 540 nm using a microplate reader [45].

4.8 | In Vitro Photothermal Response of Scaffolds Under NIR Irradiation

The in vitro NIR-driven heating effect was assessed by immersing each scaffold in a 35 mm Petri dish containing DI water. An 808 nm NIR laser (PSU-W-FC, Changchun New Industries Co., Ltd.) with an 8 mm beam diameter was irradiated at a power density of 3 W cm^{-2} for 25 min. Temperature evolution was tracked with an infrared thermal camera (E60, FLIR), and the maximum surface temperature was documented.

4.9 | In Vivo Photothermal Response of Scaffolds Under NIR Irradiation

All animal experiments were approved by the Institutional Animal Care and Use Committee of the Korea Institute of Medical Microrobotics (KIMIRo-IACUC-2025-R-002). The in vivo photothermal response was assessed using 8-week-old male Balb/c mice. Following shaving of the abdominal region, a lower midline incision was performed to expose the peritoneal cavity, and the scaffold was implanted. An 808 nm NIR laser (beam diameter: 8 mm; PSU-W-FC, Changchun New Industries Co., Ltd.) was irradiated onto the abdominal region containing the implanted scaffold at a power density of 1 W cm^{-2}. Real-time temperature variation at the maximum heating point was monitored using an infrared thermal camera (E60, FLIR).

4.10 | Drug Loading and Release Behavior

PTX was loaded into the PCL–ZrO_2 composite by co-dissolving the composite and PTX (10 wt% relative to PCL) in a small volume of DCM. The resulting solution was precipitated in diethyl ether and subsequently filtered. After vacuum drying for 1 day at 23 °C, the PTX-loaded composite was directly processed into 3D-printed scaffolds or membranes without further purification. Following PDA coating, the drug release profile of PTX-loaded PDA@PCL–ZrO_2 was investigated under natural release and NIR-triggered stimulation conditions. Disc-shaped PTX-loaded membranes (each ~22 mg in mass and ~1 cm in diameter) were immersed in 5 mL of 1× PBS (pH 7.2). For natural release, each membrane was placed in a 20 mL glass vial and incubated at 37 °C. At defined time points (2, 4, 24 h, and 4 days), aliquots of the release medium were collected, and the membrane was transferred into 5 mL of fresh PBS to continue the release. The experiment was concluded at day 4 once saturation was achieved, and the medium was quantitatively monitored throughout to confirm the absence of drug precipitation. For NIR-triggered release, the sample was immersed in PBS in a Petri dish and incubated at 37°C. Irradiation was performed using an 808 nm laser at a power density of 3 W cm^{-2}. Each irradiation cycle comprised 5 min of laser exposure followed by a 30 min rest period. Following each rest period, the release medium was collected and replaced with 5 mL of fresh PBS to initiate the next cycle. This process was repeated for a total duration of approximately 300 min. The released PTX concentration was quantified by HPLC. Each 1.5 mL PBS aliquot was mixed with 0.15 mL of an anisole solution (10 mg mL^{-1}) as an internal standard. PTX quantification was conducted using an isocratic mobile phase comprising H_2O and acetonitrile (50:50, v/v).

4.11 | NIR-Triggered Drug Release Tests on Cells

HUVECs (3×10^3 cell/well) and VSMCs (1×10^4 cell/well) were cultured in a 48-well plate using Bronchial Epithelial Cell Growth Medium (BEBM) supplemented with SingleQuot Kit Suppl & Growth Factors or Dulbecco's Modified Eagle Medium (DMEM), respectively, both containing 10% fetal bovine serum (FBS). A PTX-loaded (2 wt%) PDA@PCL–ZrO_2 membrane (surface area, 0.5 cm × 0.5 cm) was introduced into the respective cell media and irradiated with NIR light for 10 min per day at a power density of 3 W cm^{-2}. After irradiation, the eluted media were collected, filtered, and added to the cells following the removal of the spent media. The membrane was then washed with PBS, air-dried, and reused for subsequent irradiations. Cell viability was evaluated after 1, 3, and 7 NIR exposure cycles. Non-irradiated samples served as controls.

4.12 | Cell Chemotaxis

Transwell assays were conducted to assess the migration of VSMCs. During these assays, a 100 μL suspension of the VSMCs (2×10^5 cells mL^{-1}) was added to inserts with a pore size of 8 μm [46]. The lower chambers were filled with 600 μL of PBS (control), full culture media, or full media containing PTX-loaded (2 wt%) PDA@PCL–ZrO_2 scaffolds. The detailed setup for each condition was as follows (upper chamber/lower chamber): (i) HUVECs and VSMCs at a 1:1 ratio/PBS; (ii) HUVECs and VSMCs at a 1:1 ratio/BEBM and DMEM (1:1, v/v); (iii) HUVECs and VSMCs at a 1:1 ratio/BEBM, DMEM, and scaffold sample; (iv) VSMCs/DMEM; (v) VSMCs/DMEM and scaffold sample. Cell

16136829, 2026, 61, Downloaded from https://onlinelibrary.wiley.com/doi/10.1002/smll.75502 by Sogang University, Wiley Online Library on [04/11/2026]. See the Terms and Conditions (https://onlinelibrary.wiley.com/terms-and-conditions) on Wiley Online Library for rules of use; OA articles are governed by the applicable Creative Commons License

migration proceeded for 24 h. Thereafter, cells in the upper chamber were removed using a cotton swab. Migrated cells were rinsed with PBS, fixed in 4% paraformaldehyde, permeabilized with methanol, and stained with Giemsa (Sigma) following the manufacturer's protocol. Stained cells were then examined using an optical microscope (Nikon Eclipse Ti2).

4.13 | Effect of NIR Irradiation on Intimal Hyperplasia

To assess the effects of NIR irradiation on cell viability in the absence of PTX, VSMCs were seeded onto PDA@PCL–ZrO_2 films (surface area: 0.5 cm × 0.5 cm) at a density of 2×10^5 cells mL^{-1} and incubated for 24 h before irradiation at 3 W cm^{-2} for 10 min. Cell morphology was monitored at each time point using the same optical microscope.

Acknowledgements

This research was supported by Basic Science Research Program through the National Research Foundation of Korea (NRF) funded by the Ministry of Education (No. RS-2025-25404226), and by an NRF grant funded by the Korea government (MSIT) (Nos. 2020R1A5A8018367 and RS-2024-00334734).

Funding

This research was supported by Basic Science Research Program through the National Research Foundation of Korea (NRF) funded by the Ministry of Education (No. RS-2025-25404226), and by an NRF grant funded by the Korea government (MSIT) (Nos. 2020R1A5A8018367 and RS-2024-00334734).

Conflicts of Interest

The authors declare no conflicts of interest.

Data Availability Statement

The data that support the findings of this study are available from the corresponding author upon reasonable request.

References

1. F. Liu, Y. Wang, J. Cao, et al., "A Simple Method for Fabricating Polymer/Ceramic Functionally Graded Material Scaffold," *Ceramics International* 50, no. 9 (2024): 14497–14512, https://doi.org/10.1016/j.ceramint.2024.01.362.

2. W. Zhang, M. Yu, Y. Cao, et al., "An Anti-bacterial Porous Shape Memory Self-adaptive Stiffened Polymer for Alveolar Bone Regeneration After Tooth Extraction," *Bioactive Materials* 21 (2023): 450–463, https://doi.org/10.1016/j.bioactmat.2022.08.030.

3. L. J. Tan, W. Zhu, and K. Zhou, "Recent Progress on Polymer Materials for Additive Manufacturing," *Advanced Functional Materials* 30, no. 43 (2020): 2003062, https://doi.org/10.1002/adfm.202003062.

4. D. O. Golubchikov, A. K. Petrov, V. A. Popkov, P. V. Evdokimov, and V. I. Putlayev, "Advances in the Fabrication of Polycaprolactone-Based Composite Scaffolds for Bone Tissue Engineering: From Chemical Composition to Scaffold Architecture," *ACS Biomaterials Science & Engineering* 11, no. 6 (2025): 3201–3227, https://doi.org/10.1021/acsbiomaterials.5c00205.

5. Y. J. Jeong, B. Choi, S. Kim, et al., "Fully Bioresorbable, all-polymer-based, 3D-printed Scaffolds With Prolonged Radiopacity and Enhanced Durability," *Chemical Engineering Journal* 494 (2024): 152851, https://doi.org/10.1016/j.cej.2024.152851.

6. C. Tian, S. Zhang, V. Lloveras, and J. V. Gancedo, "Application of Radical Dendrimers as Organic Radical Contrast Agents for Magnetic Resonance Imaging," *Advanced Industrial and Engineering Polymer Research* 7, no. 2 (2024): 255–261, https://doi.org/10.1016/j.aiepr.2023.07.001.

7. Q. Wang, X. Yu, X. Chen, et al., "A Facile Composite Strategy to Prepare a Biodegradable Polymer Based Radiopaque Raw Material for "Visualizable" Biomedical Implants," *ACS Applied Materials & Interfaces* 14, no. 21 (2022): 24197–24212, https://doi.org/10.1021/acsami.2c05184.

8. C. K. Emonde, M. E. Eggers, M. Wichmann, C. Hurshler, M. Ettinger, and B. Denkena, "Radiopacity Enhancements in Polymeric Implant Biomaterials: A Comprehensive Literature Review," *ACS Biomaterials Science & Engineering* 10, no. 3 (2024): 1323–1334, https://doi.org/10.1021/acsbiomaterials.3c01667.

9. F. Hahn, A. F. Montero, M. Queri, et al., "Electroactive 4D Porous Scaffold Based on Conducting Polymer as a Responsive and Dynamic in Vitro Cell Culture Platform," *ACS Applied Materials & Interfaces* 16, no. 5 (2024): 5613–5626, https://doi.org/10.1021/acsami.3c16686.

10. P. Feng, R. Zhao, W. Tang, et al., "Structural and Functional Adaptive Artificial Bone: Materials, Fabrications, and Properties," *Advanced Functional Materials* 33, no. 23 (2023): 2214726.

11. P. Zahedifar, R. Morent, S. Aliakbarshirazi, R. Ghobeira, and N. D. Geyter, "Enhancement of the Bio-Responsiveness of PCL Nanofibers via the Combination of a Thiol Plasma-Polymerized Coating and Fibronectin Immobilization," *Applied Surface Science Advances* 27 (2025): 100752, https://doi.org/10.1016/j.apsadv.2025.100752.

12. S. Kar, R. S. Das, T. Bera, et al., "A Custom-Engineered Water-Soluble Peptide-Based Macrocyclic Polynuclear Gd3+-Chelated Paramagnetic Multimodal Contrast Agent for Mitochondria-Targeted Fluorescence Imaging Integrated With MRI," *Analytical Chemistry* 97, no. 42 (2025): 23183–23195, https://doi.org/10.1021/acs.analchem.5c03379.

13. S. Rizzuti, E. Rosa, E. D. Gregorio, et al., "Multicomponent Peptide and Iron(III)-based Hydrogel Scaffolds: Enhanced MRI Detection for Biomedical Applications," *International Journal of Pharmaceutics* 679 (2025): 125749, https://doi.org/10.1016/j.ijpharm.2025.125749.

14. I. Chatzaki and M. Gkikas, "Osteoarthritis/Inflammation in Vitro Detection Using a Hyaluronate-Coated Au Nano-Contrast Probe," *ACS Applied Nano Materials* 7, no. 9 (2024): 10194–10204, https://doi.org/10.1021/acsanm.4c00657.

15. C. Meng, X. Liu, R. Li, et al., "3D Poly (L-lactic Acid) Fibrous Sponge With Interconnected Porous Structure for Bone Tissue Scaffold," *International Journal of Biological Macromolecules* 268 (2024): 131688, https://doi.org/10.1016/j.ijbiomac.2024.131688.

16. J. Wu, C. Jiao, H. Yu, et al., "3D printed Barium Titanate/Calcium Silicate Composite Biological Scaffold Combined With Structural and Material Properties," *Biomaterials Advances* 158 (2024): 213783, https://doi.org/10.1016/j.bioadv.2024.213783.

17. P. Cai, C. Li, Y. Ding, et al., "Elastic 3D-Printed Nanofibers Composite Scaffold for Bone Tissue Engineering," *ACS Applied Materials & Interfaces* 15, no. 47 (2023): 54280–54293, https://doi.org/10.1021/acsami.3c12426.

18. B. Chen, Z. Lin, Q. Saiding, et al., "Enhancement of Critical-Sized Bone Defect Regeneration by Magnesium Oxide-Reinforced 3D Scaffold With Improved Osteogenic and Angiogenic Properties," *Journal of Materials Science & Technology* 135 (2023): 186–198, https://doi.org/10.1016/j.jmst.2022.06.036.

19. L. Zhu, S. Jia, T. Liu, et al., "Aligned PCL Fiber Conduits Immobilized With Nerve Growth Factor Gradients Enhance and Direct Sciatic Nerve Regeneration," *Advanced Functional Materials* 30, no. 39 (2020): 2002610, https://doi.org/10.1002/adfm.202002610.

16136829, 2026, 61, Downloaded from https://onlinelibrary.wiley.com/doi/10.1002/smll.75502 by Sogang University, Wiley Online Library on [04/11/2026]. See the Terms and Conditions (https://onlinelibrary.wiley.com/terms-and-conditions) on Wiley Online Library for rules of use; OA articles are governed by the applicable Creative Commons License

20. C. H. Jang, M. S. Kim, Y. B. Cho, Y. S. Jang, and G. H. Kim, "Mastoid Obliteration Using 3D PCL Scaffold in Combination With Alginate and rhBMP-2," *International Journal of Biological Macromolecules* 62 (2013): 614–622, https://doi.org/10.1016/j.ijbiomac.2013.10.011.

21. R. Huang, C. Hu, S. Xu, et al., "3D-Printed Bifunctional Scaffold for Treatment of Critical Bone Defects Based on Osteoimmune Microenvironment Regulation and Osteogenetic Effects," *ACS Applied Materials & Interfaces* 16, no. 46 (2024): 63345–63357, https://doi.org/10.1021/acsami.4c15212.

22. M. Delemeester, K. M. Pawelec, J. M. L. Hix, et al., "Device Design and Advanced Computed Tomography of 3D Printed Radiopaque Composite Scaffolds and Meniscus," *Advanced Functional Materials* 34, no. 44 (2024): 2404860, https://doi.org/10.1002/adfm.202404860.

23. S. Mansi, S. V. Dummert, G. J. Topping, et al., "Introducing Metal–Organic Frameworks to Melt Electrowriting: Multifunctional Scaffolds With Controlled Microarchitecture for Tissue Engineering Applications," *Advanced Functional Materials* 34, no. 2 (2024): 2304907, https://doi.org/10.1002/adfm.202304907.

24. Y. Shen, C. Tang, B. Sun, et al., "Development of 3D Printed Biodegradable, Entirely X-Ray Visible Stents for Rabbit Carotid Artery Implantation," *Advanced Healthcare Materials* 13, no. 15 (2024): 2304293.

25. J. Chen, Y. Huang, L. Deng, et al., "Preparation and Research of PCL/Cellulose Composites: Cellulose Derived From Agricultural Wastes," *International Journal of Biological Macromolecules* 235 (2023): 123785, https://doi.org/10.1016/j.ijbiomac.2023.123785.

26. N. Doostmohammadi, M. Yousefpour, M. S. Nourbakhsh, and M. Bahraminasab, "Fabrication and Characterization of 3D Printed PCL/ZrO2/FA Scaffolds for Bone Tissue Engineering," *Materials Chemistry and Physics* 338 (2025): 130659, https://doi.org/10.1016/j.matchemphys.2025.130659.

27. Y. Wu, W. Zhou, L. Zhou, et al., "Near-infrared Photothermal Effect Enhanced Heterogeneous Catalysis of Co3O4/PDA Composite for Highly Efficient Activation of Peroxymonosulfate to Degrade Antibiotic Pollutants," *Chemical Engineering Journal* 474 (2023): 145267, https://doi.org/10.1016/j.cej.2023.145267.

28. Z. N. Zhuang, Y. D. Qi, Q. X. Huang, et al., "Storable Polydopamine Nanoparticles Combined With Bacillus Calmette-Guérin for Photothermal-Immunotherapy of Colorectal Cancer," *Advanced Functional Materials* 34, no. 39 (2024): 2404381, https://doi.org/10.1002/adfm.202404381.

29. W. Lin, J. Zhang, G. Pan, et al., "Multifunctional Wide-Temperature Threshold Conductive Eutectic Hydrogel Sensor for Shoulder Pain Monitoring and Photothermal Therapy," *Advanced Functional Materials* 35, no. 49 (2025): 09779, https://doi.org/10.1002/adfm.202509779.

30. Q. S. Kahdim, Z. Benzarti, M. H. Mousa, M. H. Rasheed, N. Abdelmoula, and A. Khalfalah, "Enhancing the Multifunctional Properties of Polycaprolactone/Chitosan Films With Zirconium Dioxide Nanoparticles for Biomedical and Flexible Optoelectronic Applications," *RSC Advances* 15, no. 38 (2025): 31788–31805.

31. J. E. Kim, Y. H. Yun, H. Park, et al., "Hydrogen-Bonded QSEBS/ZrO2 Mixed Matrix Anion Exchange Membranes for Water Electrolyzer," *Fuel* 376 (2024): 132684, https://doi.org/10.1016/j.fuel.2024.132684.

32. R. Qie, S. Z. Moghaddam, and E. Thormann, "Dopamine-Assisted Layer-by-Layer Deposition Providing Coatings With Controlled Thickness, Roughness, and Functional Properties," *ACS Omega* 8, no. 3 (2023): 2965–2972, https://doi.org/10.1021/acsomega.2c05620.

33. Y. J. Jeong, S. Jeong, S. Kim, et al., "3D-printed Cardiovascular Polymer Scaffold Reinforced by Functional Nanofiber Additives for Tunable Mechanical Strength and Controlled Drug Release," *Chemical Engineering Journal* 454 (2023): 140118, https://doi.org/10.1016/j.cej.2022.140118.

34. Z. Yang, M. Liu, Y. Yang, et al., "Biofunctionalization of Zirconia With Cell-adhesion Peptides via Polydopamine Crosslinking for Soft Tissue Engineering: Effects on the Biological Behaviors of human Gingival Fibroblasts and Oral Bacteria," *RSC Advances* 10, no. 11 (2020): 6200–6212.

35. A. S. Vijayan, A. Joseph, A. Joseph, T. S. Abhijith, B. G. Nair, and V. Sajith, "Polydopamine Functionalised Ceria-zirconia Nanoparticles Embedded Water-borne Epoxy Nanocomposite for Anti-Biofouling Coatings," *Progress in Organic Coatings* 187 (2024): 108094, https://doi.org/10.1016/j.porgcoat.2023.108094.

36. M. V. Sivasankar, M. L. Chinta, and P. S. Rao, "Zirconia Based Composite Scaffolds and Their Application in Bone Tissue Engineering," *International Journal of Biological Macromolecules* 265 (2024): 130558, https://doi.org/10.1016/j.ijbiomac.2024.130558.

37. T. Liang, L. Zeng, Y. Shi, et al., "In Vitro and in Vivo Antibacterial Performance of Zr & O PIII Magnesium Alloys With High Concentration of Oxygen Vacancies," *Bioactive Materials* 6 (2021): 3049–3061, https://doi.org/10.1016/j.bioactmat.2021.02.025.

38. A. V. Finn, M. Nakazawa, J. Joner, et al., "Pathological Correlates of Late Drug-Eluting Stent Thrombosis," *Circulation* 115 (2007): 2435–2441, https://doi.org/10.1161/CIRCULATIONAHA.107.693739.

39. M. Joner, A. V. Finn, A. Farb, et al., "Pathology of Drug-Eluting Stents in Humans," *Journal of the American College of Cardiology* 48 (2006): 193–202, https://doi.org/10.1016/j.jacc.2006.03.042.

40. Z. Wang, J. Guo, X. Han, et al., "Metformin represses the pathophysiology of AAA by suppressing the activation of PI3K/AKT/mTOR/autophagy pathway in ApoE−/− Mice," *Cell & Bioscience* 9 (2019): 68, https://doi.org/10.1186/s13578-019-0332-9.

41. Y. T. Wu, L. Chen, Z. B. Tan, et al., "Luteolin Inhibits Vascular Smooth Muscle Cell Proliferation and Migration by Inhibiting TGFBR1 Signaling," *Frontiers in Pharmacology* 9 (2018): 1059, https://doi.org/10.3389/fphar.2018.01059.

42. N. Wu, C. Ye, F. Zheng, et al., "MiR155-5p Inhibits Cell Migration and Oxidative Stress in Vascular Smooth Muscle Cells of Spontaneously Hypertensive Rats," *Antioxidants* 9, no. 3 (2020): 204.

43. Y. L. Yu, J. J. Wu, C. C. Lin, et al., "Elimination of Methicillin-resistant Staphylococcus aureus Biofilms on Titanium Implants via Photothermally-triggered Nitric Oxide and Immunotherapy for Enhanced Osseointegration," *Military Medical Research* 10, no. 21 (2023): 21, https://doi.org/10.1186/s40779-023-00454-y.

44. Y. Deng, J. Huang, C. Chen, Y. Wen, and D. Qiu, "Fe_3O_4 Coated Stent Prevent Artery Neointimal Hyperplasia by Inhibiting Vascular Smooth Muscle Cell Proliferation," *Materials Today Bio* 27 (2024): 101133, https://doi.org/10.1016/j.mtbio.2024.101133.

45. D. Zhang, L. Mei, Y. Hao, et al., "A Hydrogel-Based First-Aid Tissue Adhesive With Effective Hemostasis and Anti-bacteria for Trauma Emergency Management," *Biomaterials Research* 27 (2023): 56, https://doi.org/10.1186/s40824-023-00392-9.

46. S. Jin, X. Qi, B. Zhang, et al., "Evaluation of Promoting Effect of a Novel Cu-Bearing Metal Stent on Endothelialization Process From in Vitro and In Vivo Studies," *Scientific Reports* 7 (2017): 17394, https://doi.org/10.1038/s41598-017-17737-9.

Supporting Information

Additional supporting information can be found online in the Supporting Information section.

Supporting File: smll75502-sup-0001-SuppMat.pdf.

16136829, 2026, 61, Downloaded from https://onlinelibrary.wiley.com/doi/10.1002/smll.75502 by Sogang University, Wiley Online Library on [04/11/2026]. See the Terms and Conditions (https://onlinelibrary.wiley.com/terms-and-conditions) on Wiley Online Library for rules of use; OA articles are governed by the applicable Creative Commons License